IEEE Access
Multidisciplinary | Rapid Review | Open Access Journal

Received October 19, 2020, accepted October 22, 2020, date of publication October 26, 2020, date of current version November 6, 2020.

Digital Object Identifier 10.1109/ACCESS.2020.3033527

Design of Tunable Metasurface Using Deep Neural Networks for Field Localized Wireless Power Transfer

HUU NGUYEN BUI, JIE-SEOK KIM, AND JONG-WOOK LEE, (Senior Member, IEEE)
Information and Communication System-on-Chip (SoC) Research Center, School of Electronics and Information, Kyung Hee University, Yongin 17104, South Korea

Corresponding author: Jong-Wook Lee (jwlee@khu.ac.kr)

This work was supported by the National Research Foundation of Korea under Grant 2018R1A2A2A05018621 and Grant 2020M3H2A107678611.

ABSTRACT Wireless power transfer (WPT), a convenient method for powering multiple devices, enables a truly wireless connection, eliminating the need for periodic charging and replacing a battery. To further enhance WPT, the unique characteristics of metamaterial, such as its field focusing and evanescent wave amplification, have been successfully utilized. With subwavelength characteristics, computational challenges arise when the number of metamaterial unit cells is increased. In this work, we investigate a deep neural network (DNN)-based design of the tunable metamaterial for WPT. Using structures specifically designed for different tasks, the DNN predicts the frequency spectra and synthesizes the unit cell's design parameters. When trained using a set of ∼23 000 randomly selected designs, we achieve an accumulated mean square error (MSE) of less than 1.5×10^{-3} for 97.3% of the 1929 test set. For synthesizing the unit cell's design parameters, the MSE is less than 2.5×10^{-3} for 95.7% of the test set. The data-driven method is further extended to a generative adversarial network (GAN) to create the WPT paths and predict the frequency spectra of them. To achieve high efficiency, we propose a cost function focusing on the spectra's transmission peak. After training using 80 000 measured data, the GAN can create WPT paths that efficiently connect the transmitter and the receiver on the metasurface. The results show that the DNN provides an alternative and efficient design method for the metamaterial, replacing traditional EM-simulation-based approaches.

INDEX TERMS Wireless power transfer, tunable metamaterial, metasurface, field localization, deep neural network, generative adversarial network.

I. INTRODUCTION

Wave propagation control has played a fundamental role in generating, transferring, and utilizing energy [1]. Photonic bandgap (PBG) has been utilized to confine and guide electromagnetic waves (light) using waveguides, cavity resonance, and emission control [2]. The introduction of metamaterial marks another significant step up in progress for wave control.

Metamaterials are artificial composites that exhibit unusual physical properties such as negative permittivity and permeability [3], which are not found in natural materials. The metamaterial is usually constructed using locally resonant unit cells in the deep subwavelength scale [4]. Unlike PBG materials based on Bragg interferences of periodic unit cells, the physical characteristics of metamaterial originate from overall averaged material properties. New methods for wave propagation control using metamaterials have been introduced with Pendry and Smith's pioneering work. The imaging immediately found new applications using the metamaterial's negative reflective index, which allows overcoming the resolution limit beyond classical optics, i.e., a perfect lens [5]. In addition to imaging, metamaterials have shown great potential in innovative applications such as field focusing, beam shaping, steering, and cloaking. The universal scaling property of metamaterials provides great potential for a broad range of applications. Great efforts have been put forth to seek the metamaterial applications across the whole electromagnetic (EM) spectrum from radio-frequency (RF) to near-infrared.

In this ubiquitously connected world, one wire remains necessary to supply power. Although the battery provides a way to replace the power cable, wireless power transfer (WPT) can enable a truly wireless connection without the need for periodic charging and eventual replacement of the battery. Recently, the unique characteristics of metamaterial,

The associate editor coordinating the review of this manuscript and approving it for publication was Shah Nawaz Burokur.

such as field focusing, evanescent wave amplification, and strong EM resonance (or coupling), have been successfully utilized for WPT [6]–[8] and energy harvesting [9]. For example, the use of metamaterials enables extending WPT distance [6], [7] and mitigates the effect of coil misalignment [8]. Besides, there has been significant interest in a tunable metamaterial, which can dynamically change its material parameters [10], [11]. The metamaterial consists of subwavelength unit cells as its constituent element; the metamaterial design can be computationally challenging when the number of cells is increased, when the dimension is increased, or when tunability is added. Therefore, one crucial question is how to efficiently design and characterize tunable metamaterials containing a multitude of unit cells.

The deep neural network (DNN) has recently made significant progress in achieving decision accuracy beyond the human level. Starting from a simple convolutional neural network for image classification [12], the DNN has been extended for use in many different fields such as speech recognition [13], face detection [14], and video recognition [15]. The effectiveness of optimally selecting actions, even for a search space that was believed impossible to explore, has been demonstrated [16]. Then, it has penetrated other disciplines, such as materials science, biology, biomedicine, medical diagnosis, and physics.

In this trend, the DNN can provide a great opportunity to extend the design and control of metamaterial. Instead of the traditional approach of solving Maxwell's equations, the data-driven model of the DNN learns from the data based on physical principles. The DNN generates output using simple arithmetic computation. Indeed, this new approach has provided a potent tool in the design of metamaterials [17]–[24]. For example, the DNN has been successfully used for predicting the optical response of chiral metamaterials [19]. A generative model of the DNN has successfully replaced the conventional trial-and-error approaches for the inverse design of the metasurface [20], [22], [24]. These results show the good potential of the DNN to replace time-consuming EM simulations, which are conducted case-by-case for each geometry.

Inspired by the paradigm shift, we investigate a DNN-based design of the tunable metamaterial for future intelligent WPT. Using the DNN, we aim to complete four tasks related to the metasurface design for WPT. The first task is using the DNN for predicting the frequency spectra of the metamaterial unit cell for a given geometry. The second task is to synthesize the design parameters of the unit cell for a given frequency spectrum. The third task is generating an efficient WPT path connecting a transmitter (Tx) and a receiver (Rx). For this task, we train the network containing multiple DNNs using 80000 measured data. To generate the high-efficiency path, we propose a cost function that focuses on the spectra's transmission peak. The fourth task is predicting the frequency spectra of the generated WPT path. Using extensive training, the DNN can successfully predict the spectra and create WPT paths that efficiently connect Tx and Rx. The contribution of this paper can be summarized as follows: we propose a DNN-based design approach to deal with the computational challenge in the metamaterial design. And we demonstrate that the DNN provides an alternative and efficient design method for metamaterial, which can replace the traditional approach using the EM solver. Applying the DNN to WPT will stimulate advanced WPT research, and our work will be useful for efficient metamaterial design future intelligent WPT.

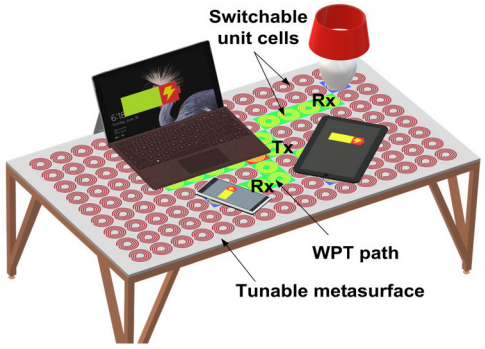

FIGURE 1. Concept of the WPT charging table realized using tunable metasurface. The metasurface consists of multiple receivers on the table that can be powered simultaneously from a transmitter. The metasurface dynamically localizes the power into the selected WPT path using switchable unit cells.

II. FIELD-LOCALIZED WAVEGUIDE ON METASURFACE

Metamaterials constructed using a grid of split-ring resonators (SRRs) have been investigated for one-dimensional (1D) arrays [25] and two-dimensional (2D) waveguides [26]. Because the previous works are developed mainly for data transfer, the energy is not well confined inside the waveguide; the high losses are not suitable for WPT. The metamaterial-based cavities can better confine the fields to reduce the loss [27]. This concept of field localization is further extended for a resonator-coupled WPT to increase efficiency [28]. In this work, we modify the cavity mode concept to create a new type of low-loss waveguide on the tunable metasurface.

Fig. 1 shows an artist's rendering of the WPT charging table realized using the tunable metasurface. Previously, a smart table based metasurface was reported for WPT [7]. The table embedded in the desktop was realized using a group of wires underneath the dielectric resonators, which play the role of a channel connection between Tx and Rx. Our approach is similar to the previous work [7] in that multiple devices can be powered simultaneously, regardless of the location on the table. However, the physical principle is quite different. The proposed method is realized by using cavity mode enabled for field localization [29] and dynamically localizes power into the WPT path using switchable unit cells.

To realize the dynamically switchable function, we embed a nonlinear element in the cell and further extend the functionality of the cavity. The nonlinear varactor allows the creation of the tunable cavity mode by shifting the resonance frequency. This results in a non-uniform metasurface, where the unit cells are modified locally to control the wave propagation [1]. Because the overall material property

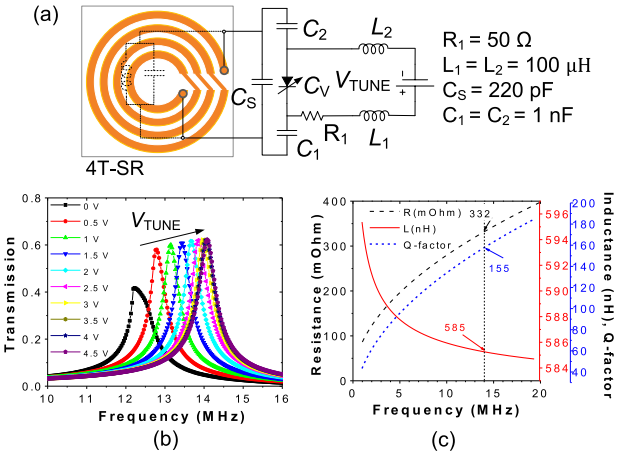

FIGURE 2. (a) Schematic of the switchable unit cell, (b) transmission related to the resonance frequencies of the unit cell for various V_{TUNE}, (c) the resistance, the inductance, and the Q factor of the unit cell as a function of frequency.

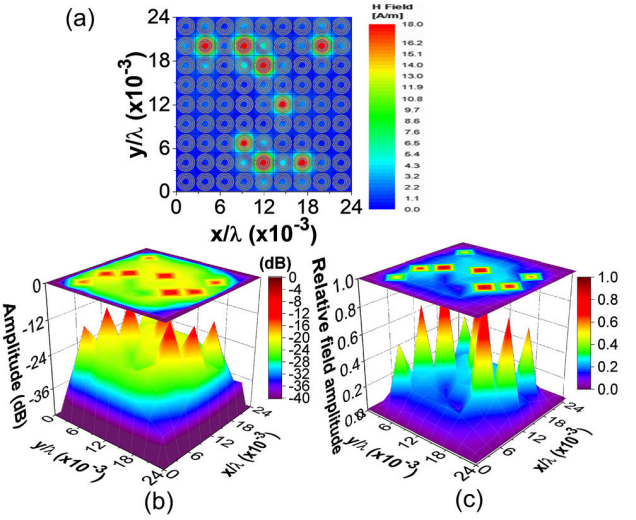

FIGURE 3. (a) Simulated field intensity distribution on metasurface, (b) measured field amplitude obtained by scanning over the metasurface at z = 0.5 cm, (c) field amplitude in the relative scale.

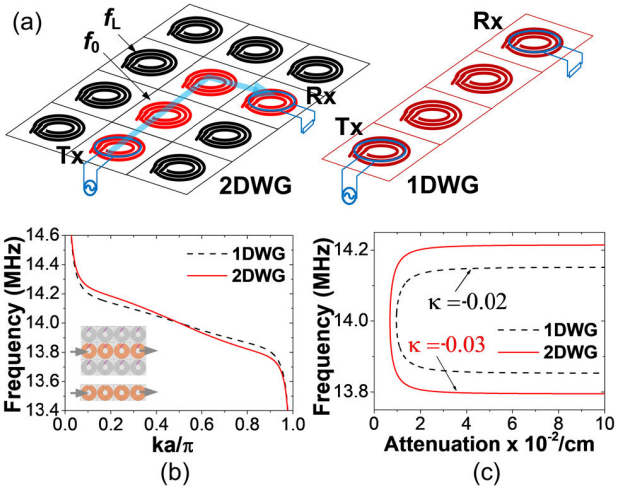

FIGURE 4. (a) Schematic of the waveguides, (b) measured dispersion characteristics of the waveguides, (c) attenuation as a function of frequency.

governs the physical property of the metamaterial, unit cell modification does not significantly change its property [30]. Fig. 2(a) shows the schematic of the switchable unit cell, which is realized using a four-turn spiral resonator (4T-SR) and tuning elements. The dimension of the 4T-SR is similar to the one used in the previous work [29]. The varactor C_V provides a variable capacitance from 4 to 81 pF. The total capacitance $C_{total} = C_S + (1/C_1 + 1/C_2 + 1/C_V)^{-1}$ can be varied by controlling V_{TUNE}, which tunes the resonant frequency of the 4T-SR. Fig. 2(b) shows the measured transmission coefficient $|S_{21}|$ of the unit cell for various V_{TUNE}. The resonant frequency at $V_{TUNE} = 0$ and 4.5 V are $f_L = 12.5$ MHz and $f_0 = 14$ MHz, respectively. When the unit cell is activated ($V_{TUNE} = 4.5$ V), there is a passband at around f_0 while a stopband is formed at f_L. When the cell is turned off ($V_{TUNE} = 0$ V), the locations of the two bands interchange. Using the two distinct resonant frequencies, we create switchable unit cells to form various WPT paths. Fig. 2(c) shows the Q-factor of the unit cell as a function of frequency, which exceeds 150 at f_0.

Fig. 3(a) shows the field intensity distribution when the cavities are created on the metasurface. We choose 9×9 arrays of unit cells in this work, considering the simulation time and fabrication labor. In the charging table (Fig. 1), there will be a larger number of coils (unit cells) considering the practical desktop size. The unit cells forming the cavity resonate at f_0 while the surrounding cells resonate at f_L. The result shows that we can create a highly confined cavity mode on the metasurface. The field confinement inside the cavity can be explained using a hybridization bandgap (HBG) created by the metamaterial [1]. When the resonant frequency of surrounding cells falls into the HBG, the negative permeability of metamaterial forms a stopband for the cavities. Then, the waves are prohibited from propagating in an area other than the cavities. Fig. 3(b) shows measured field amplitude obtained by scanning over the metasurface. The field amplitude in the relative scale is shown in Fig. 3(c). The cavity region shows a relative field strength higher than 15.

Fig. 4(a) shows the 2D waveguide (2DWG) created using an array of unit cells operating at f_L and f_0. The unit cells forming the waveguide resonate at f_0 while the surrounding cells resonate at f_L. Also shown is the 1D waveguide (1DWG), where energy is transferred to nearby cells through magnetic coupling without surrounding cells. In both cases, small probes are used to couple Tx and Rx cells. In WPT, maximum power is transferred to the load when the Tx and Rx have the same frequency. All the unit cells in the WPT path have the same V_{TUNE}; therefore, they have a similar resonant frequency.

Fig. 4(b) shows the dispersion characteristics. Both 2DWG and 1DWG show backward propagation property of metamaterial. The proposed 2DWG is based on the idea that the dispersion characteristics can be engineered to confine the magneto-inductive waves (MIWs) into a subwavelength cavity. The MIW is a type of slow-wave created by

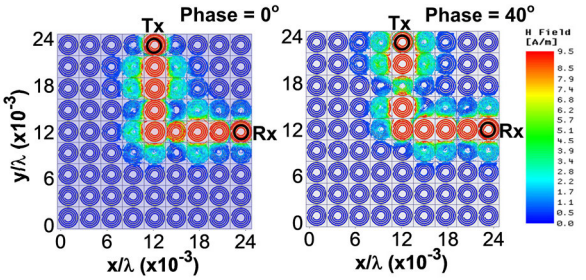

FIGURE 5. Field intensity distributions in the bender shape WPT path.

inter-element couplings [31], [32]. Therefore, the proposed method is different from the previous approach of spoof surface plasmons with the coupled defect mode [33]. Fig. 4(c) shows the attenuation as a function of frequency. The attenuation shows the minimum at f_0, which increases towards the band edge. Because the fields are better confined inside the waveguide through the cavity mode, 2DWG shows smaller attenuation than 1DWG. The coupling coefficient κ is also shown. The measured κ value of 2DWG is -0.03 for the unit having cell size $a = 6$ cm.

By reconfiguring the switchable unit cells, we create various shapes of WPT paths such as linear, diagonal, and bender on the metasurface. Fig. 5 shows the field distribution in the bender shape WPT path. The result confirms backward wave propagation. Unlike the previous approach [34], we note that the result is achieved without structural changes.

III. DEEP NEURAL NETWORKS FOR METASURFACE BASED WPT

A. DEEP NEURAL NETWORKS FOR UNIT CELL

Fig. 6(a) shows the schematic of the unit cell realized using the 4T-SR. The substrate material is FR-4. We consider six design parameters: the width W, the spacing S, the metal thickness t_m, the dielectric thickness t_d, cell size a, and the capacitor C_S. The thickness of the desk (Fig. 1) is the sum of t_d and a cover layer. The t_d is related to WPT efficiency. The cover layer, such as glass or wood, is used to avoid direct contact between the object and the unit cell. When this layer is a thin and non-magnetic material, its effect on efficiency is negligible.

Fig. 6(b) shows four examples of the unit cell having a different W. Fig. 6(c) shows transmission as a function of frequency for different W. Table 1 shows the design parameters of the unit cell. When we consider all the combinations of the parameters, there are 3.4×10^{11} designs. Among them, we randomly select 25000 samples. Using the EM solver Ansoft HFSS, we setup simulations to collect 23071 (92.28%) and 1929 (7.72%) samples for training and test sets, respectively. Each data set consists of 201 point transmission spectra over 4 MHz bandwidth. In addition to the train and test set, the validation set can be assigned for optimizing hyperparameters such as learning rate, batch size, and network structure. Because the validation set reduces the available training data, it is not used in this work. Instead, we divide the sampled data into different training

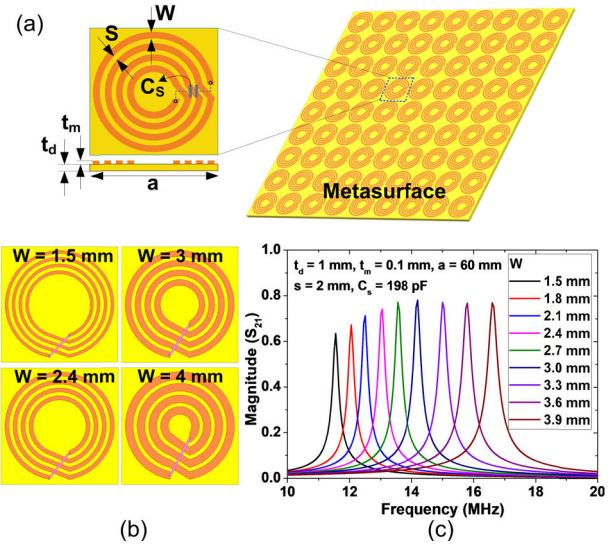

FIGURE 6. (a) Schematic of the unit cell realized using 4T-SR, (b) four examples of the unit cell having different widths, (c) simulated transmission as a function of frequency for different widths.

TABLE 1. Design parameters of the unit cell.

	Min. value	Max. value	Step	No. of cases
C_S (pF)	100	1,200	0.1	11,000
a (mm)	60	70	0.1	101
W (mm)	1	3.2	0.1	23
S (mm)	1	3.2	0.1	23
t_m (mm)	0.05	0.2	0.01	16
t_d (mm)	0.5	4	0.1	36

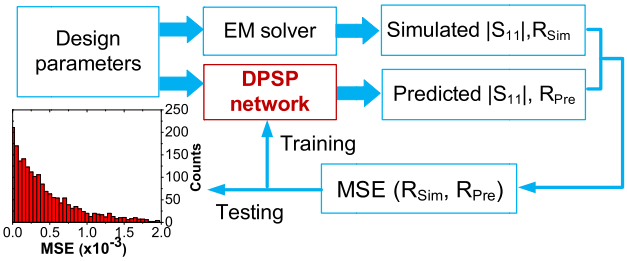

FIGURE 7. Training and testing process of the DPSP network for predicting the reflection coefficient.

and testing sets, assuring that the hyperparameters are not overfitted.

For the design of the unit cell, we use two fully-connected networks (FCNs), which are the design parameter to S-parameter (DPSP) and the S-parameter to design parameter (SPDP) networks. Both FCNs have nine layers with 1024 nodes. Fig. 7 shows the training and testing process of the DPSP network. Given the six design parameters, the DPSP network generates a 201 point reflection coefficient $|S_{11}|$. The EM solver's output is used to calculate the mean square error (MSE) for training the DPSP network. The MSE is a standard error estimator as

$$\mathrm{MSE}(a, b) = \frac{1}{n}\sum_{i}^{n}(a-b)^2. \quad (1)$$

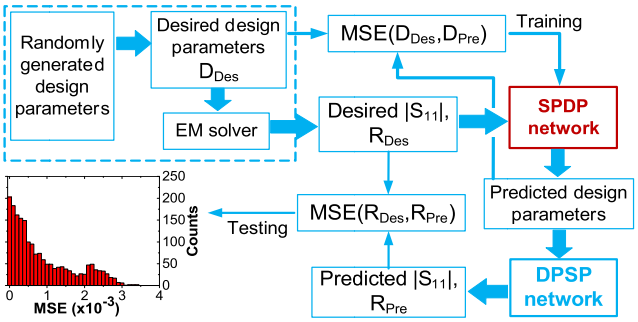

FIGURE 8. Training and testing process of the SPDP network for synthesizing the design parameters of the unit cell.

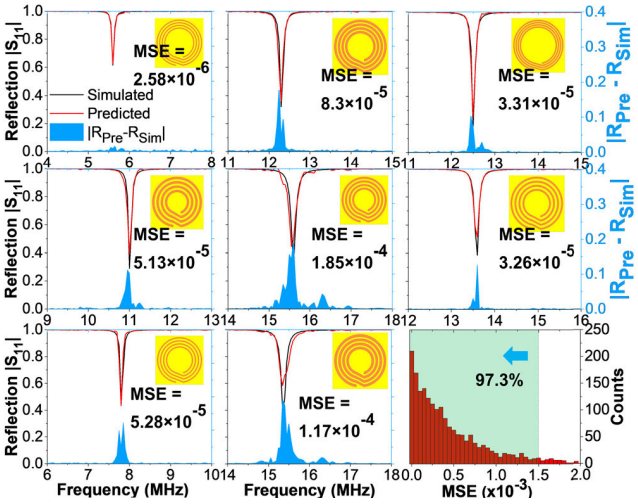

FIGURE 9. Examples of test data obtained using the DPSP network. The MSE is listed in each sub-figure. The shaded blue area shows the absolute value of the difference between the predicted and simulated reflections on the right vertical axis. A histogram of the MSE for all the test sets is also shown, where 97.3% of the test set have MSE < 1.5×10^{-3}, as indicated by the dashed vertical line.

The DPSP network and the EM solver generate the predicted (R_{Pre}) and simulated (R_{Sim}) reflection coefficients, respectively, to calculate the test error. Fig. 8 shows the training and testing process of the SPDP network. Given the desired $|S_{11}|$, the SPDP network generates the predicted design parameters (D_{Pre}), which are compared with the desired design parameters (D_{Des}) for training. The D_{Pre} is input to the already trained DPSP network to calculate the desired reflection coefficients (R_{Des}), and the test error is obtained.

Fig. 9 shows the examples of test data for the DPSP network after 2500 epoch. For each sub-figure, the MSE is also shown. When we accumulate the MSE of the 1929 test set, 97.3% of them have MSE $< 1.5 \times 10^{-3}$. The results show that the proposed approach using the DNN faithfully reconstructs the reflection spectra. Fig. 10 shows the example of a test set for the SPDP network after the 2500 epoch. When we accumulate the MSE of the 1929 test data, 95.7% of them have MSE $< 2.5 \times 10^{-3}$. These results show that the DNN can be efficiently used for synthesizing the dimension of the metamaterial unit cell. Table 2 shows the comparison

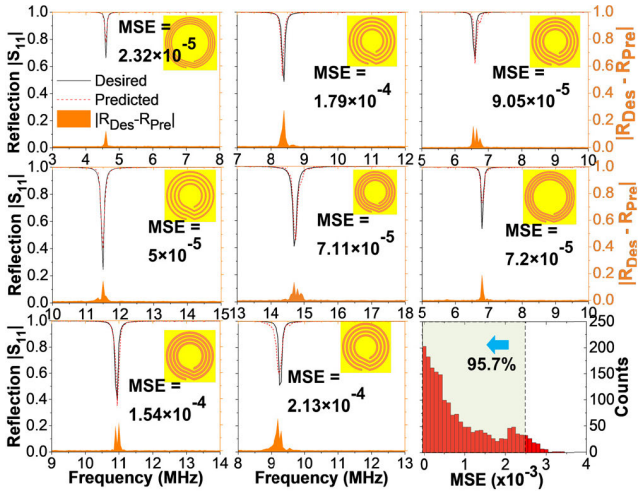

FIGURE 10. Examples of test data obtained using the SPDP network. The MSE is listed in each sub-figure. The shaded orange area shows the absolute value of the difference between the predicted and desired reflections on the right vertical axis. A histogram of the MSE for all the test sets is shown, where 95.7% of them have MSE < 2.5×10^{-3}, as indicated by the dashed vertical line.

TABLE 2. Comparison with similar studies.

	[18]	[19]	[20]	[21]	[24]	This work
No. sample	755000	30000	6500	21000	10000	25000
Test set	5000	5000	1000	3000	1000	1929
No. layer	6	9	6	9	6	9
MSE	0.19	8×10^{-4}	<0.01	1.16×10^{-3}	0.29	9×10^{-4}
DNN structure	FCN	FCN+ CONV	CONV +GAN	FCN + CONV	FCN +CONV/ VAE	FCN / CONV +GAN*

*used for WPT path generation

with similar studies. Because each work studies a specific physical phenomenon using a different DNN structure, direct comparison is difficult; using one of the largest DNN layers, our work achieves a relatively small MSE of 9×10^{-4} using 25000 samples.

We choose one design among the synthesized unit cell and fabricate the metasurface for experimental WPT demonstration. The design parameters of the unit cell, which are identical for the Tx and Rx, are $W = 3$ mm, $S = 1$ mm, $t_{\text{m}} = 0.05$ mm, $t_{\text{d}} = 0.5$ mm, $a = 60$ mm, and $C_{\text{S}} = 220$ pF. The inductance of the 4T-SR is $L = 585$ nH, and the number of turns is four. Because both the thickness (t_{d}) and periodic dimension (a) are much smaller than the wavelength of the operating frequency $f_0 = 14$ MHz, the proposed structure belongs to metamaterial.

B. DEEP NEURAL NETWORKS FOR WPT

Fig. 11(a) shows the grid map ($9 \times 9 \times 2$), which consists of binary data for the Tx and Rx locations, obstacles, and WPT paths. After we set the Tx and Rx, obstacles of four different sizes (1×1, 1×2, 2×1, and 2×2) are randomly generated using a binomial distribution. Fig. 11(b) shows the experimental setup used to collect the training data. The python code executed in a Keysight E5063A network

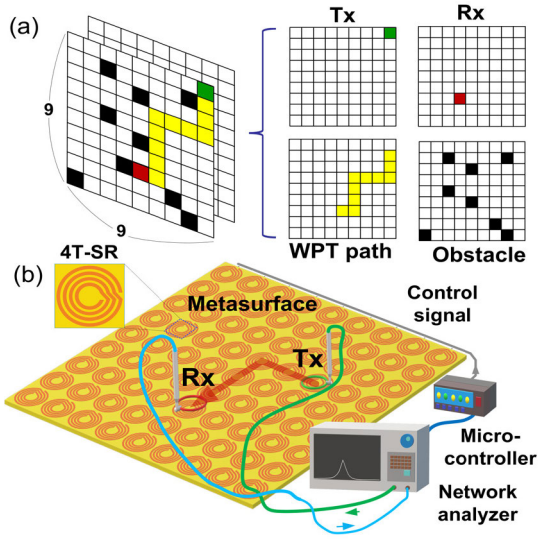

FIGURE 11. (a) Schematic of the grid map used to represent the metasurface. (b) Experimental setup to collect the training data.

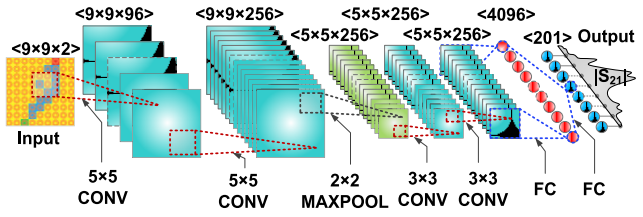

FIGURE 12. Structure of the DNN for predicting the frequency spectra of the WPT path.

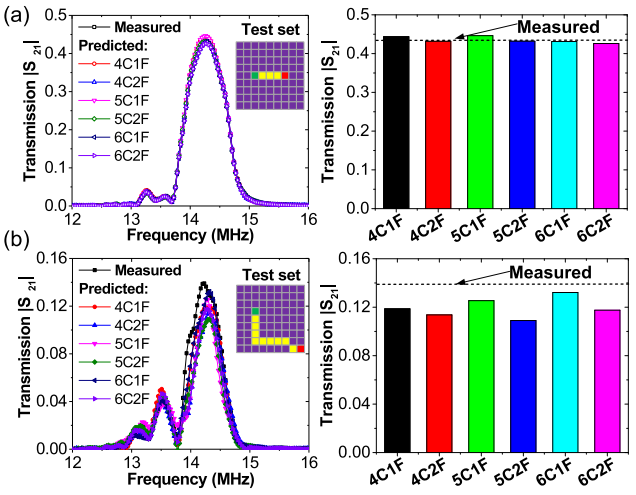

FIGURE 13. Comparison of measured and predicted transmission obtained using different DNNs. (a) Straight, (b) 'L' shape paths.

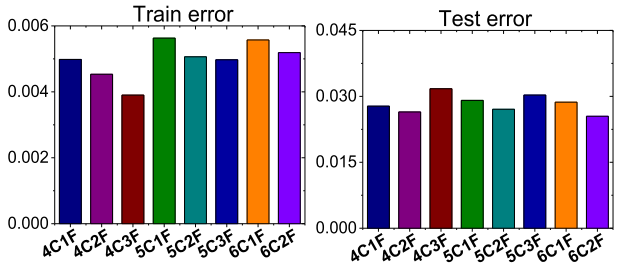

FIGURE 14. Histogram of the training and test errors achieved by the different DNNs.

analyzer generates various paths between the Tx and Rx. A microcontroller interfaced with the network analyzer activates the unit cells to generate the WPT path. For each generated path, $|S_{21}|$ data are collected by the analyzer.

The quality and the number of training data can significantly affect the test error. When arbitrary random paths are generated, the paths most likely result in a relatively low $|S_{21}|$. Besides, the obstacle generates cases where no path exists between the Tx and Rx. These low-quality data can result in longer training time for the DNN and increase the test error. To obtain quality training data closely related to the goal (or achieving a high transmission), we perform preprocessing using the heuristics pathfinding algorithm A* [35]. Using A*, we check whether there exists a path connecting between the Tx and Rx. To further increase the chance of generating high transmission paths, we modify A* by adding a random value (between 0 and 1) to the calculated heuristic cost. Using this method, we collect 80000 training sets and 500 test sets. Each data set consists of 201 point transmission over 4 MHz bandwidth.

Fig. 12 shows the structure of the DNN, predicting the frequency spectra of the path or Predictor (See Table 4). The input to the Predictor is the grid map. The output has 201 nodes, each representing the magnitude of $|S_{21}|$ in 32b floating-point format. To investigate the performance depending on the DNN structure, we test several Predictors, which have four to six convolutional (CONV) layers and having one to two fully-connected (FC) layers. For example, 4C2F represents the network having four CONV layers and two FC layers. Each CONV layer includes a rectified linear unit (ReLU) as an activation function.

Fig. 13(a) shows the prediction results obtained using different DNNs for a straight-shaped path. The result shows that all the networks predict the measured data faithfully. The worst-case error at peak transmission is 2.3% when the 5C1F structure is used. Fig. 13(b) shows the result for the 'L' shape path, and the 6C1F structure shows the lowest error. Fig. 14 shows the histogram of the train and test errors achieved by different DNNs. The result is obtained at 200 epoch by averaging the MSE of all the train and test sets. The 4C3F structure shows the lowest train error; this structure shows a relatively poor test error attributed to overfitting. Considering the error and complexity, we choose the 4C2F structure. Fig. 15(a) shows the examples of the measured and predicted transmission of the WPT paths chosen among the training set. The training is performed using the 4C2F network. Fig. 15(b) compares the measured and predicted results selected among the test set. The results show that the transmission spectra of the path are faithfully reconstructed over the 4 MHz bandwidth.

The above results are obtained by the DNN trained using the MSE(T_M, T_P) over 201 frequency points, where T_M is the measured transmission, and T_P is predicted transmission. Therefore, the result focuses on fitting the predicted to the

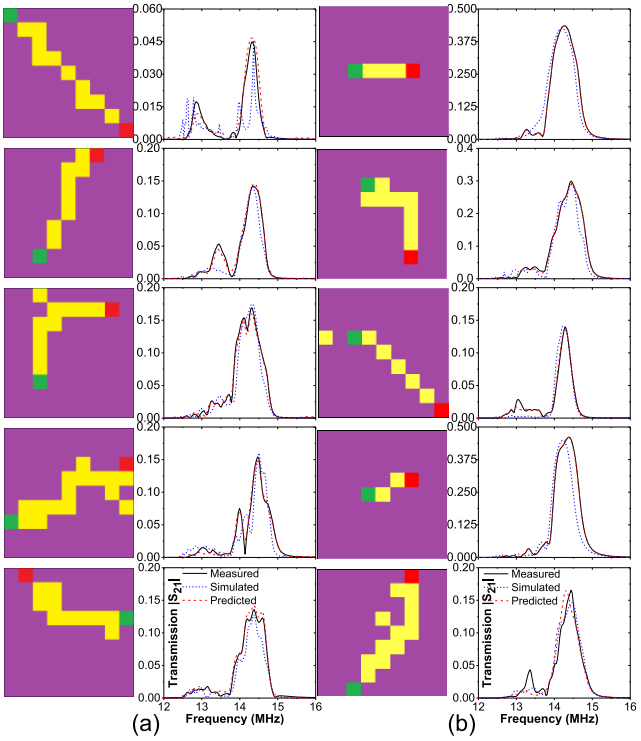

FIGURE 15. Comparison between the measured and predicted transmissions for the arbitrarily generated paths. (a) Training set, (b) test set. The waveguide is shown in each sub-figure, where green, red, yellow squares indicate Tx, Rx, and WPT path, respectively.

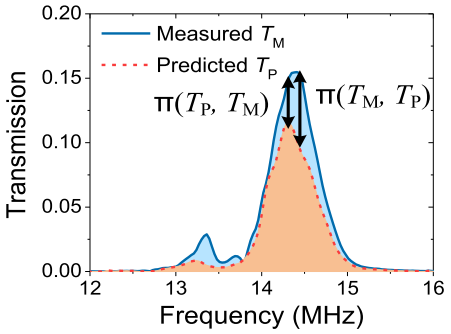

FIGURE 16. An example of the measured and predicted transmission.

measured data over the 4 MHz bandwidth. Because WPT is usually performed using a narrow frequency band, accurate prediction of the peak transmission with the associated frequency is important. Fig. 16 shows one example of the measured and predicted transmission spectra. We observe two peaks, one measured and the other predicted. The $\Pi(x, y)$ represents the error at the peak point as

$$\Pi(x, y) = \text{MSE}\left\{x\left[\text{argmax}(x)\right], y\left[\text{argmax}(x)\right]\right\} \quad (2)$$

where argmax returns the point at which the function value is the maximum. The $\Pi(T_M, T_P)$ represents the MSE computed at the single frequency where T_M is the maximum. Similarly, $\Pi(T_P, T_M)$ is the MSE at the frequency where T_P is the highest. To make a clear demonstration of the DNN for practical WPT application, we train the Predictor to focus on the peak. For this purpose, we minimize the modified cost

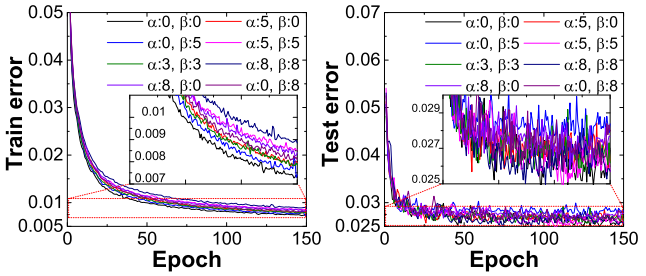

FIGURE 17. Train and test errors of the predictor for different α and β.

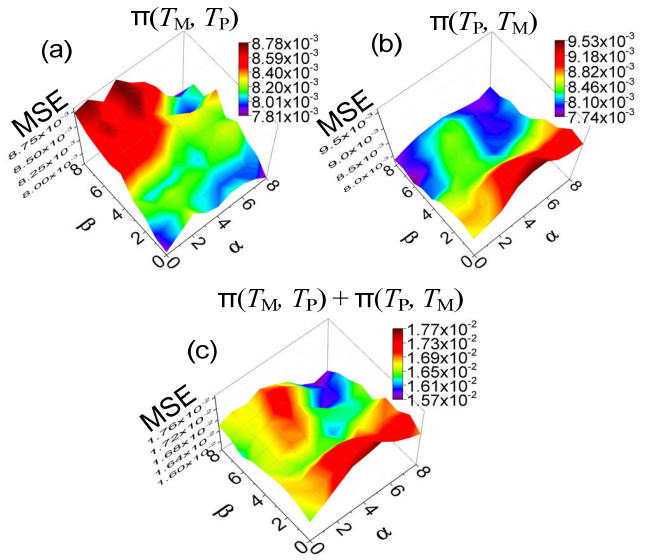

FIGURE 18. (a) Plot of Π (T_M, T_P) as a function of α and β, (b) plot of Π (T_P, T_M) as a function of α and β, (c) combined results.

function $C_\Pi(T_M, T_P)$ as

$$C_\Pi(T_M, T_P) = \min\left[\text{MSE}(T_M, T_P) + \alpha \cdot \Pi(T_M, T_P) + \beta \cdot \Pi(T_P, T_M)\right] \quad (3)$$

where the two parameters α and β are used to assign the weight for the two peaks.

Fig. 17 shows the train and test errors obtained using the different α and β. The result shows that error is slightly reduced when the value of α or β increases, but its effect on both errors is relatively small, which is an expected result; the MSE(T_M, T_P) is computed using 201 points while α and β affect only two points. These results show that the Predictor can be successfully trained using C_Π with the variables α and β. We can observe the effect of α and β by considering the narrow region around the peak. Fig. 18(a) shows $\Pi(T_M, T_P)$ as a function of α and β. The result shows that $\Pi(T_M, T_P)$ decreases with increasing α and decreasing β. Fig. 18(b) shows $\Pi(T_P, T_M)$ as a function of α and β, which decreases with increasing β. To choose suitable α and β, we combine the two results, as shown in Fig. 18(c). The result shows that a relatively small error is achieved when α and β are chosen in the range from 6 to 8.

Fig. 19 shows the computation time of the two approaches of using the EM solver and DNN. We use Ansys HFSS version 2019 for the EM solver. We use the Tensorflow

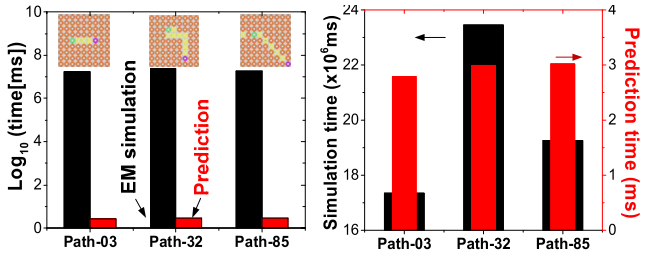

FIGURE 19. Comparison of the computation time.

version 2.0 for DNN. Both HFSS and DNN are run on the HP Z640 workstation having a 64 GB memory, a GTX1080 GPU, and a Xeon E5-1650v3 processor. When the EM solver is used, the procedure is exact, and the error is attributed to the estimated parameters such as loss tangent. When this approach is used, it takes 20×10^6 msec (5.5 hours) for each design. In the case when DNN is used, the time is reduced to 3 msec, corresponding to 6.7 million times reduction. The result shows that the DNN approach significantly reduces the computation time.

To use the DNN for the metamaterial design, we need to collect the training data, and it takes about 10 hours to train the DNN. Because the network is trained for the WPT setup using structural parameters (Table 1), it needs retraining for different structures; our design is a kind of special DNN for the WPT setup. Although there exists the overhead for the data collection and the preprocessing, we believe that the approach using the DNN is more efficient than the traditional approach using the EM solver. This is because the trained network can be reused once the optimized network is established, and the computation is based on simple arithmetic. Besides, the accumulation of the learned data can further increase the accuracy. In comparison, computation using the EM solver does not allow reusing the data by learning, and design has to be solved case-by-case for each geometry.

C. GENERATIVE ADVERSARIAL NETWORK FOR WPT

In this work, we investigate a generative adversarial network (GAN) to create the WPT path. The GAN is an unsupervised learning method that uses a Generator and a Discriminator, and this approach has shown good potential for such tasks as metasurface pattern synthesis [20], image generation [36], and video prediction [37].

Unlike the variational auto-encoder (VAE), which uses learned approximate inference [24], we use a pre-trained Predictor to seek the design goal with other networks in the GAN. We may consider reinforcement learning (RL), which has been used for various pathfinding problems. The RL is a machine learning technique where an agent interacts with the environment and decides current action to maximize overall reward [38], [39]. Because the metasurface physics is relatively complicated, it is difficult to define the agent's environment state. In the GAN, the Predictor works as an environment to train the Generator. Therefore, GAN has an advantage over RL in that it does not need the complicated physical model of the metasurface.

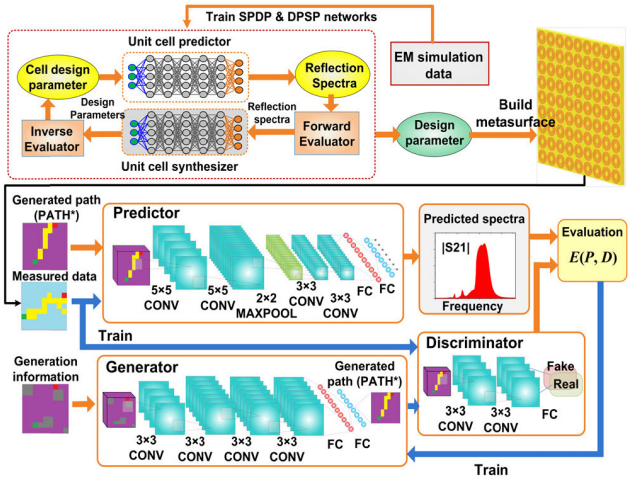

FIGURE 20. Block diagram of the overall neural network. The GAN includes a generator, a predictor, and a discriminator. The GAN generates the WPT path and predicts the frequency spectra. Two FCNs are used for predicting the frequency spectra and generating the design parameters of the unit cell.

TABLE 3. Layer parameters of the generator.

Layer		Feature	Size	Kernel	Stride
Input		2	9×9	-	-
1	Convolution	128	9×9	5×5	1
2	Convolution	256	9×9	5×5	1
3	Convolution	256	9×9	5×5	1
4	Convolution	256	9×9	5×5	1
5	Convolution	128	9×9	5×5	1
Output	Fully-connected	-	81	-	-

Fig. 20 shows the block diagram of the overall neural network. Two FCNs (SPDP and DPSP networks) predict the reflection spectra, and they synthesize the design parameters of the unit cell. The GAN consists of three sub-networks: a Generator, a Predictor, and a Discriminator. They are specifically designed for different purposes. The role of the Generator is to produce a real-like output so that it is classified as real by the Discriminator. The Discriminator decides whether its input is made-up (or generated) or real data. Two networks are trained alternately through competitive learning, and the Generator continues to produce a refined output.

The data input to the GAN includes g_k, r_k, and d_k. The g_k is the generation information for $9 \times 9 \times 2$ feature map (See Fig. 11). The r_k represents the map containing the measured path. The d_k is the known ground truth of the binary value (measured or generated). The Generator receives g_k to produce the output $G(g_k)$, which contains the WPT path data between Tx and Rx. After testing several networks, we choose the 4C2F structure without the max-pooling layer, which shows a better result. This may be attributed to the already dense $9 \times 9 \times 2$ map, which contains g_k and the path information. Table 3 shows the layer parameters of the Generator. Batch normalization is not used considering the computational overhead. The Predictor receives r_k for training, and it outputs the predicted transmission spectra $P(G(g_k))$, which contains 201 points float32 value. The Predictor uses the 4C2F structure (Table 4). To train the Generator so that

TABLE 4. Layer parameters of the predictor.

Layer		Feature	Size	Kernel	Stride
Input		2	9×9	-	-
1	Convolution	96	9×9	5×5	1
2	Convolution	256	9×9	5×5	1
3	Max-pooling	256	5×5	2×2	2
4	Convolution	256	5×5	3×3	1
5	Convolution	256	5×5	3×3	1
6	Fully-connected	-	4096	-	-
Output	Fully-connected	-	201	-	-

TABLE 5. Layer parameters of the discriminator.

Layer		Feature	Size	Kernel	Stride
Input		2	9×9	-	-
1	Convolution	32	9×9	5×5	1
2	Convolution	32	9×9	5×5	1
Output	Fully-connected	-	-	-	-

it produces a path having a high transmission, we use the training loss as

$$-\frac{1}{N}\sum_{k=0}^{N}\log[\max(P(G(g_k)))] \tag{4}$$

where the max function outputs the peak value of the predicted transmission. Because the gradient of log function decreases with the value, it helps to stabilize the training.

The Discriminator receives either r_k or $G(g_k)$ and outputs the true or false binary result. The output of the Discriminator is used to train the Generator so that it continues to generate improved WPT paths. Because the Discriminator performs a relatively simple task, we use a 2C1F structure (Table 5). When training the Discriminator, it is desirable to maximize $D(r_k)$ when d_k is true. Similarly, $D(G(g_k))$ needs to be minimized for the input $G(g_k)$, or d_k is false. The cross-entropy loss is widely used for its advantage of providing fast training. When most of $G(g_k)$ is classified as real by the Discriminator, the cross-entropy loss can show saturation in improving $G(g_k)$ by the vanishing gradient. To directly penalize the decision error, we use the least-squares loss [40] as

$$\frac{1}{N}\sum_{k=0}^{N}[D(G(g_k)) - d_k]^2 \quad \text{while } d_k = 0. \tag{5}$$

where $N = 50$ is the batch size for training chosen by considering our computing memory size. When the input to the Discriminator is measured data r_k (or d_k is true), the training loss is expressed as

$$\frac{1}{N}\sum_{k=0}^{N}[D(r_k) - d_k]^2 \quad \text{while } d_k = 1. \tag{6}$$

The overall system uses both the Predictor and Discriminator to train the Generator. During training, the weights of the Generator and the Discriminator are updated alternately. The iterative update algorithm of the GAN can show nonconvergent oscillation causing excessive training time. Wasserstein GAN is proposed to improve learning stability by using the loss function with Wasserstein distance (or earth-mover distance) [41]. Because the oscillation often occurs

TABLE 6. Hyperparameters for training the networks.

	Predictor	Generator	Discriminator
Learning rate	5×10^{-3} - 10^{-3}	10^{-3}	10^{-3}
Batch size	50	50	50
Optimizer	Adam*	Adam	Adam
Activation	ReLU	ReLU & Sigmoid**	ReLU & Sigmoid**
Batch norm.	N	N	N

* $\beta_1 = 0.9$, $\beta_2 = 0.999$, $\varepsilon = 10^{-8}$. ** used only in the last layer.

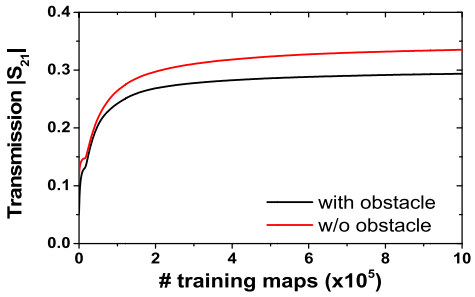

FIGURE 21. Transmission as a function of the number of maps.

when the fixed loss function is used, we add an adjustable parameter σ to avoid the issue [20]. We apply this technique in combining (4) and (5), and train the Generator using

$$\min\left[-\frac{1}{N}\sum_{k=0}^{N}\{\log[\max(P(G(g_k)))] + \sigma\log[D(G(g_k))]\}\right]. \tag{7}$$

A large value of σ forces the Generator to output the paths based on only the collected (measured) training set. By setting the appropriate value for σ, the Generator can produce a path showing high transmission, which is not included in the training set. After testing several networks, we choose $\sigma = 0.1$. Table 6 shows the hyperparameters used for training the three networks.

Fig. 21 shows the transmission as a function of the number of training maps. Two results with and without the obstacle are shown. The result is obtained by averaging the transmission of all the maps. In both cases, the transmission steadily increases with training. The case without the obstacles increases the transmission up to 0.34. When the obstacle is present, it increases to 0.29. The lower transmission with the obstacle present can be explained by the fact that longer paths are usually needed to connect Tx and Rx while also avoiding the obstacle. Considering that the transmission is 0.68 when the Tx and Rx are located right next to each other, the result indicates that relatively high-quality WPT paths are generated between the Tx and Rx. Fig. 22 shows examples of the generated path. We observe that most of the paths are connected with additional side cells, improving the transmission. Besides, we observe a few cells which are not connected from the main path; they have a relatively small effect on transmission in most cases.

Fig. 23(a) shows the experimental setup to demonstrate WPT to multiple devices. Fig. 23(b)-(d) show the experimental results. Two WPT paths are shown, which transfers

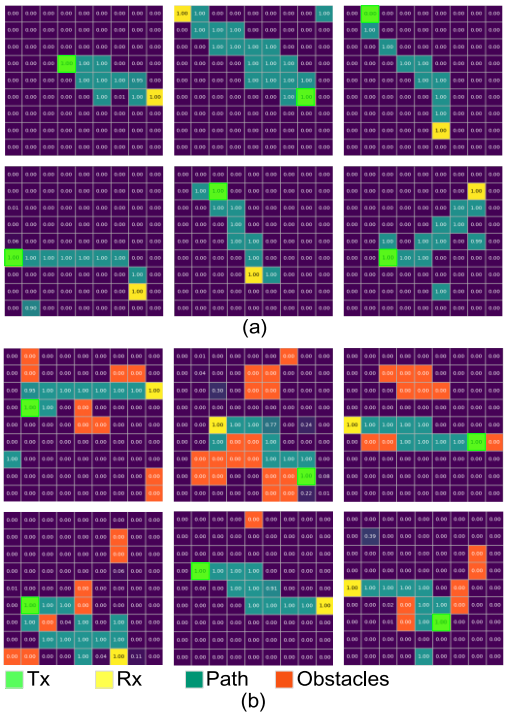

FIGURE 22. Examples of the generated WPT path (a) without (b) with the obstacles.

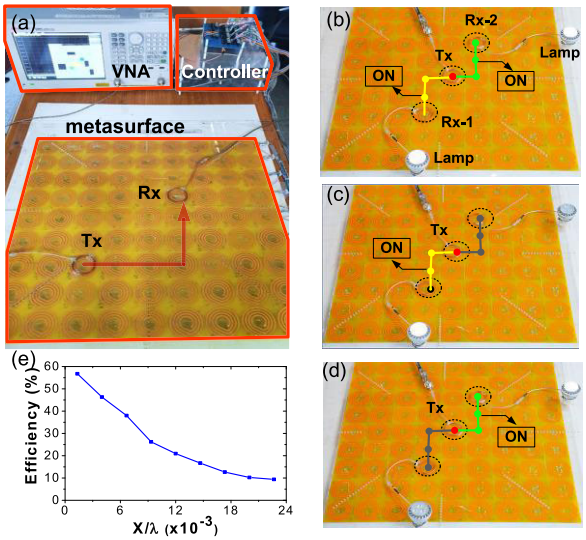

FIGURE 23. (a) Experimental setup of the proposed WPT system using tunable metasurface, (b)-(d) experimental WPT results using two LEDs, (e) measured efficiency as a function of the distance.

10 W to light-emitting diode (LED) lamps with the 4 W and 12 V specifications. The Tx is placed at the metasurface center or $(x, y) = (5, 5)$. In this experiment, Rx-1 and Rx-2, which are connected to the LED, are placed at $(x, y) = (4, 3)$ and $(6, 7)$, respectively. When the paths are created, the two LED lamps are turned on, demonstrating the proposed metasurface's successful WPT operation. Fig. 23(e) shows the measured power transfer efficiency. We obtain the efficiency of 56.8%, 46.3%, 38%, 26.2%, and 9.4% at the distance of 3 cm, 6 cm, 12 cm, 18 cm, and 48 cm, respectively. The efficiency gradually decreases when the path becomes longer or the distance between Tx and Rx is increased [42], [43].

IV. CONCLUSION

In this work, we investigate a DNN-based design of the tunable metamaterial for a future intelligent WPT. We use specifically designed DNN structures for different tasks of predicting the frequency spectra and synthesizing the design parameters of the unit cell. The DNNs are trained using 23070 randomly selected samples. For predicting the spectra, an accumulated MSE less than 1.5×10^{-3} is achieved for 97.3% of the 1929 test set. The accumulated MSE is less than 2.5×10^{-3} for 95.7% of the test set for synthesizing the unit cell's design parameters. The results show that the metamaterial unit cell can be efficiently designed with high accuracy. We further extended the data-driven methods to the GAN for creating WPT paths and predicting the frequency spectra. To achieve high efficiency, we train the DNN using a modified cost function to focus on the spectra's transmission peak. After training using 80000 measured data, the GAN creates WPT paths that efficiently connect the Tx and Rx on the metasurface. Using the generated paths, we experimentally demonstrate WPT to multiple devices. When transferring 10 W power, a peak efficiency of 56.8% is achieved. The results show that the DNN provides an alternative and efficient design method for the metamaterial, replacing the traditional EM-simulation based approaches.

REFERENCES

[1] F. Lemoult, N. Kaina, M. Fink, and G. Lerosey, "Wave propagation control at the deep subwavelength scale in metamaterials," *Nature Phys.*, vol. 9, no. 1, pp. 55–60, Jan. 2013.

[2] K. Aoki, D. Guimard, M. Nishioka, M. Nomura, S. Iwamoto, and Y. Arakawa, "Coupling of quantum-dot light emission with a three-dimensional photonic-crystal nanocavity," *Nature Photon.*, vol. 2, no. 11, pp. 688–692, Oct. 2008.

[3] V. G. Veselago, "The electrodynamics of substances with simultaneously negative values of ε and μ," *Sov. Phys. Usp*, vol. 10, no. 4, pp. 517–526, Apr. 1968.

[4] W. J. Padilla, D. N. Basov, and D. R. Smith, "Negative refractive index metamaterials," *Mater. Today*, vol. 9, nos. 7–8, pp. 28–35, Aug. 2006.

[5] J. B. Pendry, "Negative refraction makes a perfect lens," *Phys. Rev. Lett.*, vol. 85, no. 18, pp. 3966–3969, Oct. 2000.

[6] A. L. A. K. Ranaweera, T. P. Duong, and J.-W. Lee, "Experimental investigation of compact metamaterial for high efficiency mid-range wireless power transfer applications," *J. Appl. Phys.*, vol. 116, no. 4, Jul. 2014, Art. no. 043914.

[7] M. Song, K. Baryshnikova, A. Markvart, P. Belov, E. Nenasheva, C. Simovski, and P. Kapitanova, "Smart table based on a metasurface for wireless power transfer," *Phys. Rev. A, Gen. Phys.*, vol. 11, no. 5, May 2019, Art. no. 054046.

[8] A. L. A. K. Ranaweera, C. A. Moscoso, and J.-W. Lee, "Anisotropic metamaterial for efficiency enhancement of mid-range wireless power transfer under coil misalignment," *J. Phys. D, Appl. Phys.*, vol. 48, no. 45, Oct. 2015, Art. no. 455104.

[9] L. Li, X. Zhang, C. Song, and Y. Huang, "Progress, challenges, and perspective on metasurfaces for ambient radio frequency energy harvesting," *Appl. Phys. Lett.*, vol. 116, no. 6, Feb. 2020, Art. no. 060501.

[10] Y. Zhao, C. Huang, Z. Song, C. Yu, S. Liang, X. Luo, and A. Qing, "A digital metamaterial of arbitrary base based on voltage tunable liquid crystal," *IEEE Access*, vol. 7, pp. 79671–79676, Jul. 2019.

[11] W. Wang, C. Xu, M. Yan, A. Wang, J. Wang, M. Feng, J. Wang, and S. Qu, "Broadband tunable metamaterial absorber based on U-shaped ferrite structure," *IEEE Access*, vol. 7, pp. 150969–150975, Oct. 2019.

[12] Y. Lecun, L. Bottou, Y. Bengio, and P. Haffner, "Gradient-based learning applied to document recognition," *Proc. IEEE*, vol. 86, no. 11, pp. 2278–2324, Nov. 1998.
[13] A. B. Nassif, I. Shahin, I. Attili, M. Azzeh, and K. Shaalan, "Speech recognition using deep neural networks: A systematic review," *IEEE Access*, vol. 7, pp. 19143–19165, Feb. 2019.
[14] R. Qi, R.-S. Jia, Q.-C. Mao, H.-M. Sun, and L.-Q. Zuo, "Face detection method based on cascaded convolutional networks," *IEEE Access*, vol. 7, pp. 110740–110748, Aug. 2019.
[15] Y. LeCun, Y. Bengio, and G. Hinton, "Deep learning," *Nature*, vol. 521, pp. 436–444, May 2015.
[16] D. Silver, A. Huang, C. J. Maddison, A. Guez, L. Sifre, G. van den Driessche, J. Schrittwieser, I. Antonoglou, V. Panneershelvam, M. Lanctot, S. Dieleman, D. Grewe, J. Nham, N. Kalchbrenner, I. Sutskever, T. Lillicrap, M. Leach, K. Kavukcuoglu, T. Graepel, and D. Hassabis, "Mastering the game of go with deep neural networks and tree search," *Nature*, vol. 529, no. 7587, pp. 484–489, Jan. 2016.
[17] Z. Fang and J. Zhan, "Deep physical informed neural networks for metamaterial design," *IEEE Access*, vol. 8, pp. 24506–24513, Feb. 2020.
[18] D. Liu, Y. Tan, E. Khoram, and Z. Yu, "Training deep neural networks for the inverse design of nanophotonic structures," *ACS Photon.*, vol. 5, no. 4, pp. 1365–1369, Feb. 2018.
[19] W. Ma, F. Cheng, and Y. Liu, "Deep-learning-enabled on-demand design of chiral metamaterials," *ACS Nano*, vol. 12, no. 6, pp. 6326–6334, Jun. 2018.
[20] Z. Liu, D. Zhu, S. P. Rodrigues, K.-T. Lee, and W. Cai, "Generative model for the inverse design of metasurfaces," *Nano Lett.*, vol. 18, no. 10, pp. 6570–6576, Sep. 2018.
[21] C. C. Nadell, B. Huang, J. M. Malof, and W. J. Padilla, "Deep learning for accelerated all-dielectric metasurface design," *Opt. Express*, vol. 27, no. 20, pp. 27523–27535, Sep. 2019.
[22] E. S. Harper, E. J. Coyle, J. P. Vernon, and M. S. Mills, "Inverse design of broadband highly reflective metasurfaces using neural networks," *Phys. Rev. B, Condens. Matter*, vol. 101, no. 19, May 2020, Art. no. 195104.
[23] Z. Hou, T. Tang, J. Shen, C. Li, and F. Li, "Prediction network of metamaterial with split ring resonator based on deep learning," *Nanosc. Res. Lett.*, vol. 15, no. 1, pp. 1–8, Apr. 2020.
[24] W. Ma, F. Cheng, Y. Xu, Q. Wen, and Y. Liu, "Probabilistic representation and inverse design of metamaterials based on a deep generative model with semi-supervised learning strategy," *Adv. Mater.*, vol. 31, no. 35, Aug. 2019, Art. no. 1901111.
[25] C. J. Stevens, "Magnetoinductive waves and wireless power transfer," *IEEE Trans. Power Electron.*, vol. 30, no. 11, pp. 6182–6190, Nov. 2015.
[26] S. Campione, F. Mesa, and F. Capolino, "Magnetoinductive waves and complex modes in two-dimensional periodic arrays of split ring resonators," *IEEE Trans. Antennas Propag.*, vol. 61, no. 7, pp. 3554–3563, Jul. 2013.
[27] H. Caglayan, I. Bulu, M. Loncar, and E. Ozbay, "Experimental observation of subwavelength localization using metamaterial-based cavities," *Opt. Lett.*, vol. 34, no. 1, pp. 88–90, Jan. 2009.
[28] T. S. Pham, A. K. Ranaweera, V. D. Lam, and J.-W. Lee, "Experiments on localized wireless power transmission using a magneto-inductive wave two-dimensional metamaterial cavity," *Appl. Phys. Express*, vol. 9, no. 4, Mar. 2016, Art. no. 044101.
[29] A. L. A. K. Ranaweera, T. S. Pham, H. N. Bui, V. Ngo, and J.-W. Lee, "An active metasurface for field-localizing wireless power transfer using dynamically reconfigurable cavities," *Sci. Rep.*, vol. 9, no. 1, p. 11735, Aug. 2019.
[30] N. Kaina, F. Lemoult, M. Fink, and G. Lerosey, "Ultra small mode volume defect cavities in spatially ordered and disordered metamaterials," *Appl. Phys. Lett.*, vol. 102, no. 14, Apr. 2013, Art. no. 144104.
[31] O. Sydoruk, M. Shamonin, A. Radkovskaya, O. Zhuromskyy, E. Shamonina, R. Trautner, C. J. Stevens, G. Faulkner, D. J. Edwards, and L. Solymar, "Mechanism of subwavelength imaging with bilayered magnetic metamaterials: Theory and experiment," *J. Appl. Phys.*, vol. 101, no. 7, Apr. 2007, Art. no. 073903.
[32] R. R. A. Syms, I. R. Young, and L. Solymar, "Low-loss magneto-inductive waveguides," *J. Phys. D, Appl. Phys.*, vol. 39, no. 18, pp. 3945–3951, Sep. 2006.
[33] Z. Gao, F. Gao, and B. Zhang, "Guiding, bending, and splitting of coupled defect surface modes in a surface-wave photonic crystal," *Appl. Phys. Lett.*, vol. 108, no. 4, Jan. 2016, Art. no. 041105.
[34] S. Savo, N. Papasimakis, and N. I. Zheludev, "Localization of electromagnetic fields in disordered metamaterials," *Phys. Rev. B, Condens. Matter*, vol. 85, no. 12, Mar. 2012, Art. no. 121104.
[35] S. Russel and P. Norvig, *Artificial Intelligence: A Modern Approach*. Boston, MA, USA: Pearson, 2018.
[36] I. Goodfellow, J. Pouget-Abadie, M. Mirza, B. Xu, D. Warde-Farley, S. Ozair, A. Courville, and Y. Bengio, "Generative adversarial nets," in *Proc. Adv. Neural Inf. Process. Syst.*, 2014, pp. 2672–2680.
[37] W. Lotter, G. Kreiman, and D. Cox, "Unsupervised learning of visual structure using predictive generative networks," 2015, *arXiv:1511.06380*. [Online]. Available: http://arxiv.org/abs/1511.06380
[38] L. P. Kaelbling, M. L. Littman, and A. W. Moore, "Reinforcement learning: A survey," *J. Artif. Intell. Res.*, vol. 4, no. 1, pp. 237–285, Jan. 1996.
[39] R. S. Sutton and A. G. Barto, *Reinforcement Learning: An Introduction*. Cambridge, MA, USA: MIT Press, 2018.
[40] Y. Hong, U. Hwang, J. Yoo, and S. Yoon, "How generative adversarial networks and their variants work: An overview," *ACM Comput. Surv.*, vol. 52, no. 1, pp. 10:1–10:43, Feb. 2019.
[41] M. Arjovsky, S. Chintala, and L. Bottou, "Wasserstein generative adversarial networks," in *Proc. Int. Conf. Mach. Learn.*, Sydney, NSW, Australia, Aug. 2017, pp. 214–223.
[42] A. M. Jawad, H. M. Jawad, R. Nordin, S. K. Gharghan, N. F. Abdullah, and M. J. Abu-Alshaeer, "Wireless power transfer with magnetic resonator coupling and sleep/active strategy for a drone charging station in smart agriculture," *IEEE Access*, vol. 7, pp. 139839–139851, Oct. 2019.
[43] Y. Li, S. Jiang, X.-L. Liu, Q. Li, W.-H. Dong, J.-M. Liu, and X. Ni, "Influences of coil radius on effective transfer distance in WPT system," *IEEE Access*, vol. 7, pp. 125960–125968, Sep. 2019.

HUU NGUYEN BUI was born in Vietnam, in August 10, 1990. He received the B.S. degree in control engineering and automation from the Hanoi University of Mining and Geology, Vietnam, in 2013. He is currently pursuing the M.S. and Ph.D. degrees with the School of Electronics and Information, Kyung Hee University, South Korea. His research interests include wireless power transfer and metamaterials.

JIE-SEOK KIM was born in South Korea, in July 15, 1995. He received the B.S. and M.S. degrees from the School of Electronics and Information, Kyung Hee University, South Korea, in 2018 and 2020, respectively. His research interests include deep learning and digital circuits.

JONG-WOOK LEE (Senior Member, IEEE) was born in South Korea, in April 6, 1970. He received the B.S. and M.S. degrees in electrical engineering from Seoul National University, Seoul, South Korea, in 1993 and 1997, respectively.

From 1994 to 1996, he served in the military. From 1998 to 2002, he was a Research Assistant with the School of Electrical and Computer Engineering, Purdue University, West Lafayette, USA. From 2003 to 2004, he was a Postdoctoral Research Associate with the University of Illinois at Urbana–Champaign, USA. In 2004, he joined the Faculty of the School of Electronics and Information, Kyung Hee University, South Korea. His research interests include low-power sensor IC, wireless power transfer, RFID tag IC, and power management IC design.